Journal of Materials Chemistry A

ROYAL SOCIETY OF CHEMISTRY

PAPER

View Article Online
View Journal

Cite this: DOI: 10.1039/d5ta00823a

Tuning of mechanical properties of doped PbTe-based thermoelectric materials driven by intrinsic defects

Ilya V. Chepkasov, *[ab] Aleksandra D. Radina, [a] Viktor S. Baidyshev,[a] Mikhail Polovinkin, [ac] Nikita Rybin, [ac] Alexander Shapeev,[ac] Artem A. Krikorov,[a] Artem R. Oganov, [a] Zinovi Dashevsky,[d] Dmitry G. Kvashnin [e] and Alexander G. Kvashnin [a]

Received 30th January 2025
Accepted 2nd August 2025

DOI: 10.1039/d5ta00823a

rsc.li/materials-a

One of the primary factors that significantly restricts the lifetime of thermoelectric devices based on PbTe is the high brittleness of doped PbTe. There are several types of defects that are commonly observed in PbTe, which can have either a positive or negative impact. These include the substitution of Pb or Te by other atomic species to achieve n- or p-type doping, the substitution of Pb with Te (Te-rich PbTe) and *vice versa* (Pb-rich PbTe), and also Pb or Te vacancies. Experimentally, it is challenging to determine the influence of each defect on the mechanical properties at the atomic level. The focus of this study is the chemical bonding in the PbTe crystal, with substitutions of Pb by Bi (n-type) and Na (p-type), as well as Ag/Cu interstitials. Intrinsic defects are also examined, involving substitutions of Pb by Te and *vice versa*, and vacancies of Pb or Te. In order to achieve this, calculations of the elastic tensor are performed, as well as Crystal Orbital Hamilton Population (COHP) analysis, in combination with large-scale simulations of tensile deformation using deep neural network (DNN) interatomic potentials. The findings of this study provide insight into how to precisely change mechanical properties through defect formation. The results of this advanced comprehensive study can facilitate the development of high-efficiency thermoelectric generators based on PbTe.

1 Introduction

Lead chalcogenide compounds such as PbTe are efficient thermoelectric materials in the mid-temperature range (400–800 K),[1–3] hence these materials have been used in space thermoelectric generators since the 1960s. In 2006, a PbTe alloy was used to power the Mars rover.[4,5] Great improvements in the thermoelectric performance of p-type and n-type PbTe have been achieved in recent decades. In particular, a high peak figure of merit (zT_{peak}) of ~2.5 (p-type) and ~2 (n-type) and an average figure of merit (zT_{ave}) of ~1.5 (p-type) and ~1.27 (n-type) have been achieved.[6,7]

While most studies of thermoelectric materials have focused on improving energy conversion efficiency,[8–14] less attention has been paid to their mechanical properties. This is because thermoelectric devices are generally considered to be stress-free due to their lack of moving parts. However, during the operation of a thermoelectric generator, the material is subjected to strong cyclical temperature gradients, which result in various types of stress. This can cause cracking or fatigue,[15–19] which significantly limits the life of thermoelectric devices and hinders their commercial development.

The high brittleness of p-type PbTe poses a significant obstacle to the commercial use of PbTe-based thermoelectric materials. In recent years, a number of studies have examined the mechanical properties of these thermoelectric materials.[16,17,20–27] Gelbstein *et al.*[24] demonstrated that the mechanical properties of PbTe strongly depend on carrier type and concentration. Specifically, heavily doped p-type PbTe (*e.g.*, Na-doped, $p \geq 10^{20}$ cm^{-3}) exhibits brittle failure with low flexural strength and minimal ductility, while n-type PbTe retains high ductility and superior flexural strength across all carrier concentrations studied. This contrast persists despite identical charge carrier scattering mechanisms in both types.[24] Snyder *et al.*[17] found that the embrittlement of p-type PbTe is not significantly affected by the presence of grain boundaries, dopant size mismatch, or the type of Σ band bonding. Instead, its poor plasticity (or high brittleness) is attributed to the

[a]*Skolkovo Institute of Science and Technology, Bolshoy Boulevard 30, bld. 1, Moscow 121205, Russian Federation. E-mail: I.Chepkasov@skoltech.ru*

[b]*Katanov Khakas State University, 90 Lenin pr., Abakan, 655017, Russian Federation*

[c]*Digital Materials LLC, 4A Kutuzovskaya Str., Odintsovo, Moscow region, 143001, Russian Federation*

[d]*Department of Materials Engineering, Ben-Gurion University of the Negev, Beer-Sheva, Israel*

[e]*Emanuel Institute of Biochemical Physics RAS, 4 Kosygin Str., Moscow 119334, Russian Federation*

interaction of dislocations with point defects, which inhibits dislocation motion.

Investigations into the stability and mechanical properties of thermoelectric materials require the application of computational methods. These methods enable us to examine the structure and understand the main trends for improving the properties from an atomistic point of view. In our recent study,[25] it was shown that the ductile behaviour of n-type PbTe is a consequence of an excess of electrons localized on impurity atoms occupying antibonding orbitals. We carried out a detailed analysis of two cases: Bi and Sb (n-type) impurities, and Na and K (p-type) impurities, which substitute for the Pb atom in PbTe.[25] This weakens the bond, making the material more ductile. In the case of p-type doping, stronger bonds have been observed to form. This is a consequence of the bonding orbitals being fully occupied in the absence of antibonding states.

However, it is not only the dopants that influence the properties. The influence of intrinsic defects can drastically change our understanding of how mechanical properties are tuned *via* doping. The most common types of intrinsic defects are tellurium and lead vacancies (here and below, the following notations are given: vac_{Te} and vac_{Pb}), substitutions of a Pb atom by a Te atom and *vice versa* (Pb_{Te} and Te_{Pb}). These intrinsic defects primarily affect the mechanical properties of PbTe-based thermoelectric materials. In particular, it has been demonstrated[17,28] that high concentrations of point defects, such as vacancies, can lead to embrittlement and increased hardness. Snyder *et al.*[17] showed that substituting a Te atom with a Pb atom hardens PbTe, and noted that this needs to be rigorously investigated. Zhao *et al.*[29] showed that Pb vacancies promote the dissolution of Na in the PbTe matrix by increasing its doping percentage, thereby reducing the likelihood of spontaneous defect formation, such as vac_{Te} and Te_{Pb}. In addition to substitutional doping, interstitial doping is used to enhance the thermoelectric properties of PbTe. This also modifies the mechanical properties of PbTe-based thermoelectric materials. There are several types of defects observed in PbTe.[17,26,28,30–37] These involve substituting Pb or Te with other types of atoms to achieve n-type or p-type doping, as well as interstitial defects involving the incorporation of Ag or Cu atoms into the PbTe crystal structure. Experimentally, it is difficult to determine the influence of each individual defect on the mechanical properties. For example, interstitial doping of n-type Ag and Cu leads to hardening of PbTe, which is not observed with other types of n-type doping.

Therefore, we focus on the study of chemical bonding in the PbTe crystal with the following defects: (1) n-type: Pb substituted by Bi; (2) p-type: Pb substituted by Na; (3) Ag/Cu interstitials; (4) intrinsic defects: Pb_{Te}, Te_{Pb}, vac_{Pb}, and vac_{Te}. Fig. 1 schematically presents all types of considered defects. To obtain a deep insight into the changes in the mechanical behavior of doped PbTe, we perform large-scale tensile strength computations using machine learning potentials based on deep neural networks (DNNs).

2 Methods

2.1 Details of DFT calculations

All DFT calculations are carried out using the Vienna *Ab initio* simulation package (VASP) with plane-wave basis sets.[38–40] The Perdew–Burke–Ernzerhof parametrization for the exchange–correlation functional (PBEsol) is used.[41,42] Our convergence tests have shown that an energy cutoff of 300 eV achieves excellent convergence of energies, forces and stresses. The electronic self-consistency threshold is set to 1×10^{-6} eV. To

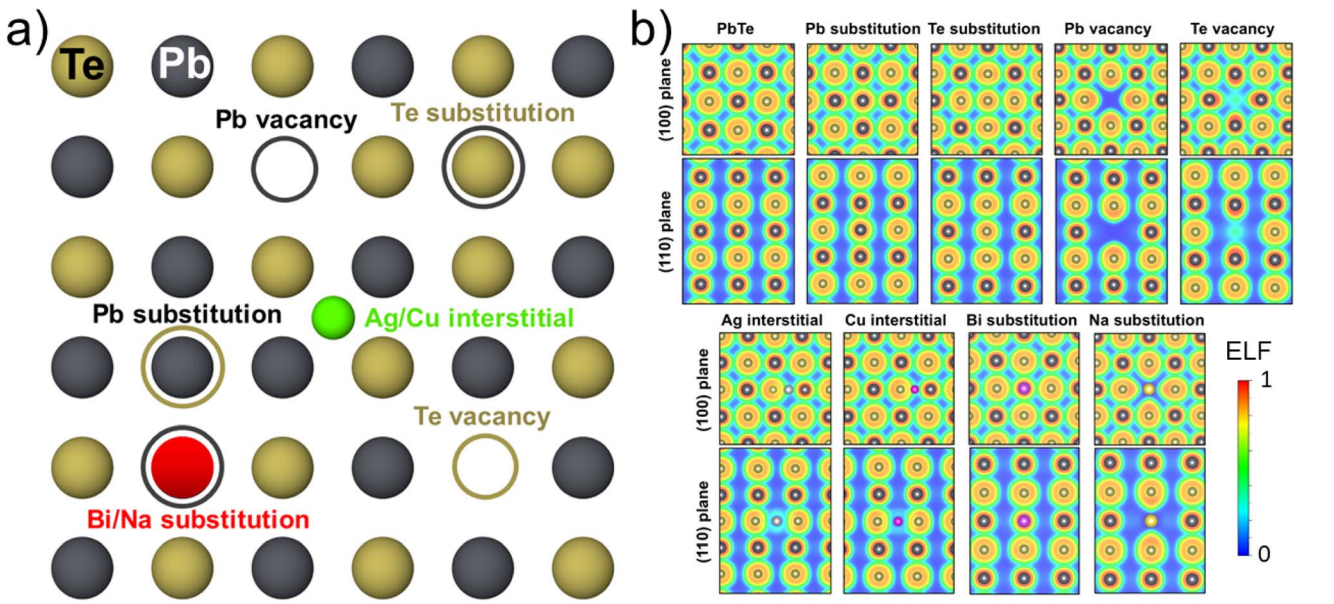

Fig. 1 (a) The crystal structure of the (100) plane of PbTe, highlighting defects such as Pb and Te vacancies, Pb and Te atom substitutions, interstitial Ag/Cu and Bi (n-type) and Na (p-type) atom substitutions. The yellow atoms represent Te and the gray atoms represent Pb. (b) The electron localization function is shown for PbTe with different types of defects.

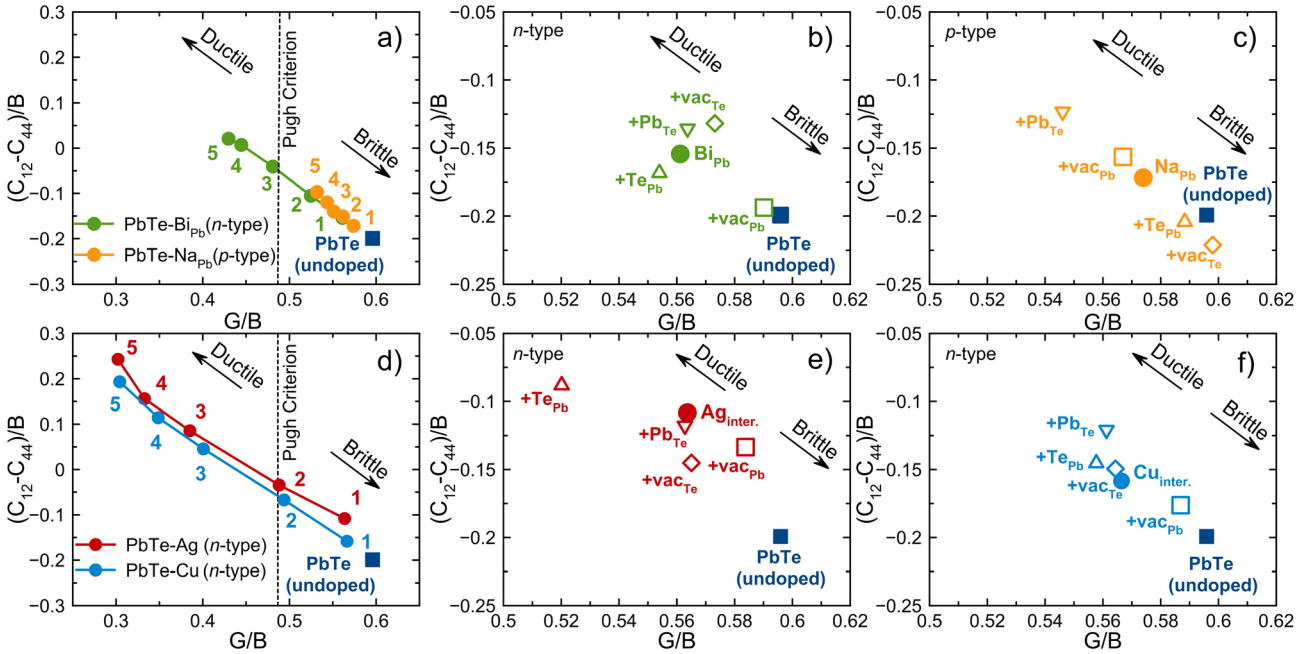

Fig. 2 The correlations between $(C_{12} - C_{44})/B$ and the Pugh ratio (G/B) are shown for the studied doped PbTe compounds, where B is the bulk modulus and G is the shear modulus. The vertical line corresponds to the Pugh–Pettifor criterion, which is calculated based on undoped PbTe. Points to the left of the line correspond to ductile materials, and points to the right correspond to brittle materials. (a) Data for Na/Bi-doped PbTe with a dopant concentration of 1–5 Na/Bi atoms per cell (216 atoms), and (b and c) additional intrinsic defects. (d) Ag/Cu interstitial doping of PbTe with concentrations ranging from 1 to 5 Ag/Cu atoms per cell (216 atoms), and (e and f) additional intrinsic defects. The considered intrinsic defects are Pb and Te vacancies (□ vac_{Pb}, ◇ vac_{Te}), and Pb and Te substitutions with Te and Pb (▽ Pb_{Te}, △ Te_{Pb}).

simulate the doped structure, we consider a PbTe supercell with a lattice parameter of $a = 19.31$ Å (108 Pb and 108 Te atoms). The Monkhorst–Pack meshes[43] $2 \times 2 \times 2$ are used to sample the first Brillouin zone of the considered PbTe (216 atoms)

For all types of point defects, the correlations between the ratio of the elastic constants $((C_{12} - C_{44})/B)$ and the Pugh ratio (G/B)[44] are calculated, as shown in Fig. 2. The elastic tensor C_{ij} is calculated from the strain ε and the stress σ using the linear relation:

$$\sigma_{ij} = \sum_{kl} C_{ijkl}\varepsilon_{kl} \tag{1}$$

2.2 Crystal orbital Hamilton population

The crystal orbital Hamilton population (COHP) method is used to study the chemical bonding between atoms in PbTe. To extract information about chemical bonding from the electronic density of states (DOS), crystal orbital overlap populations (COOPs, *i.e.* the population of mutually overlapping crystal orbitals) are used. COOPs are obtained by multiplying the DOS by the overlap population. This makes it possible to separate the total electron density into bonding and anti-bonding states. However, there are no mathematical instruments to accurately reproduce the overlap populations from the COOP, but if it could be described by the DOS, it could be described by the corresponding element of the Hamiltonian. Thus, by using the Hamiltonian, COHP was proposed as a mathematical model of populations of overlapping orbitals. The sign of COHP is the opposite of that of COOP for bonding and anti-bonding states. Therefore, –COHP diagrams are always built for clarity. COHP enables information about bonding and anti-bonding states to be obtained in a simple manner. The mathematical form of COHP is very similar to that of a projected DOS, but the density-of-states matrix is weighted by Hamilton matrix elements. For a periodic crystal, it can be defined as follows.[45]

$$\mathrm{COHP}_{AB}(\varepsilon) = \sum_{\nu\in A}\sum_{\mu\in B}\mathrm{COHP}_{\mu\nu}(\varepsilon) \tag{2}$$

$$\mathrm{COHP}_{\mu\nu}(\varepsilon) = \frac{2}{V_{BZ}}\int_{BZ} H_{\mu\nu}(k)\left\{\sum_j c^*_{\mu j}(k)c_{\nu j}(k)\delta(\varepsilon - \varepsilon_j(k))\right\}\mathrm{d}k \tag{3}$$

where $H_{\mu\nu}(k)$ is the Hamiltonian matrix in reciprocal space, $c_{\mu j}(k)$ are the expansion coefficients of the j-th occupied crystal orbital with energy $\varepsilon_j(k)$, expressed in terms of Bloch functions numbered like atomic orbitals, by the subscript μ or ν. Integration over k in eqn (2) is performed in the Brillouin zone (BZ) with a volume V_{BZ}. COHP calculations and analysis are carried out using the LOBSTER code,[46] and the contribution of each orbital to the total binding energy is considered further using the Dragon software package.

2.3 Deep neural network potential for simulation of mechanical properties

To calculate the tensile strength of the considered doped PbTe compositions, a model consisting of cylindrical PbTe rods is constructed. Each rod has a length of 200 Å and a base diameter of 50 Å, and consists of 12 480 atoms. Such cylinders are placed

in a simulation box measuring 100 × 100 × 200 Å. Periodic boundary conditions are applied only along the tensile axis Z, while the other directions are free. Prior to deformation, all cylindrical structures are relaxed to optimize the geometry and dimensions of the simulation box (using the fix box/relax command in the LAMMPS package[47,48]). The simulation of deformation consisted of resizing the simulation box along the Z-axis, followed by minimizing the geometry of the structure. The deformation step is 0.02 Å, and the simulation continues until fracture of the structure occurs. Vacancies, substitutions and interstitials are created randomly throughout the volume of the considered objects.

To describe the interatomic interactions in the considered doped structures, force field models are trained using a deep neural network (DNN) potential, as implemented in the DP-GEN package.[49] Here, the neural network is a graph neural network (GNN) combined with a feed-forward deep neural network. This contains a descriptor network (Deep Potential-Smooth Edition, DP-SE), which transforms the atomic positions of each atom into a rotation- and translation-invariant feature vector (descriptor). This uses local environment information (radial and angular information) within a cutoff radius. The second component is the fitting network (feed-forward DNN), which maps the descriptor to the atomic energy contribution. The feed-forward network typically consists of multiple hidden layers with nonlinear activation functions, and the total potential energy is represented as the sum of atomic energies to ensure extensivity (energy scales with system size).

Two DNN potentials are trained, one for PbTe doped with Bi and Na atoms and the other for PbTe containing interstitial Ag and Cu atoms. Training is performed using the DP-GEN software package,[49] which uses an active learning method to generate highly accurate interatomic potentials for multicomponent systems.[50,51] To generate the initial training set of structural configurations, *ab initio* molecular dynamics (AIMD) simulations are performed at 300 K. Each configuration is physically a slab measuring 22 × 22 × 26 Å with a thickness of 4 atomic layers and containing 128 atoms. Periodic boundary conditions are only applied along the Z-axis; while the XY-surface is considered free.

AIMD simulations of $PbTe_{1-x}Bi_x$, $PbTe_{1-x}Na_x$, $Pb_{1-x}TeBi_x$, and $Pb_{1-x}TeNa_x$ ($x = 0.0.1$) systems, which contain different types of defects (namely, vacancies and substitutions), are used to train the DNN potential that describes the mechanical properties of Bi- and Na-doped PbTe. Additional AIMD simulations are performed at 300 K for $(PbTe)_{1-x}Ag_x$ and $(PbTe)_{1-x}Cu_x$ ($x = 0.0.1$), which contain interstitial defects, in order to train the DNN potential to describe the mechanical properties of Ag- and Cu-doped PbTe. A total of 4000 atomic configurations are obtained from the AIMD simulations to train the initial DNN model. We then proceeded to active learning. To this end, we simulated the deformation (stretching) of initial PbTe slabs along the Z-axis while simultaneously selecting candidates for further training of the DNN model.

The selection of candidate structures is performed in the LAMMPS package[47,48] according to the model rejection criterion δ, which is determined by the maximum forces acting on the atoms, as calculated by different potential models.[49] According to the technique described in ref. 49, several potential models can be trained simultaneously for use in determining candidates for further training. In our case, we trained two models simultaneously. We chose a criterion whereby configurations are identified as accurate if $\delta < 0.1$ eV Å^{-1}, as failed if $\delta > 0.5$ eV Å^{-1}, and as candidates to be added to the training set in the intermediate case. Single-point DFT calculations are then performed on the selected candidate structures, allowing us to obtain the energies and forces acting on the atoms. PBEsol parametrization of the exchange-correlation functional[41,42] is used for the DFT calculations. The cut-off energy of the plane wave is set to 300 eV. The electronic self-consistency threshold is set to 1×10^{-5} eV. The first Brillouin zone is sampled using a Monkhorst–Pack mesh with a k-point grid generated with a spacing of $2\pi \times 0.25$ Å^{-1}. Training of the DNN potential, based on the configurations prepared during the active learning phase, is performed using the DeePMD-kit package.[52] The sizes of the embedding and fitting nets are set to (30, 60, 120) and (120, 120, 120), respectively. The cut-off radius is set to 7.25 Å. Each model (*i.e.* the DNN for $PbTe_{1-x}(Bi/Na)_x$ and $Pb_{1-x}Te(Bi/Na)_x$ systems, and the DNN for the $(PbTe)_{1-x}(Ag/Cu)_x$ systems) is trained with 10 000 gradient descent steps, using an exponentially decaying learning rate ranging from 10^{-4} to 10^{-8}. A total of 155 training iterations are performed during the active learning phase, incorporating an additional 6092 configurations. Correlation plots showing the relationship between DFT energies and predicted DNN energies can be found in Fig. S6 and S7 in the SI.

We used the moment tensor potential model (MTP)[53] implemented in the MLIP-2 package[54] to compute the lattice thermal conductivity (LTC) of some of the structures mentioned in this work. MTPs are generated in the active learning procedure, which is based on the D-optimality methodology and MaxVol algorithm.[55] Details of the MTP fitting procedure and LTC calculations within the scope of the Green–Kubo methodology are presented in the SI.

3 Results and discussion

To study the influence of the dopant type on the brittle behavior of PbTe, we first perform calculations on two types of substitutional defects, which have been studied in our previous work,[25] namely Bi (n-type) and Na (p-type). In contrast to the previous calculations, where a PbTe crystal with 64 atoms was studied, here we consider a PbTe crystal with 216 atoms in the supercell. This allows us to consider lower and variable defect concentrations. We consider the doping with Bi (n-type) and Na (p-type) with different concentrations. The number of Na/Bi atoms varies from 1 to 5 atoms per unit cell to see its influence on the mechanical properties of PbTe. The results are shown in Fig. 2a, where the correlations between $(C_{12} - C_{44})/B$ and the Pugh ratio are presented. It is clearly seen that PbTe becomes more ductile with both types of doping, but with increasing Bi concentration the material becomes more ductile than with increasing Na concentration (see Fig. 2a). According to our previous study[25] this comes from the excess n-type

electrons which localize on impurity atoms and occupy antibonding orbitals leading to the ductile behaviour of n-type PbTe. Increasing the excess electrons increases the ductility of PbTe.[25] However, n- and p-type doping is also accompanied by the presence of intrinsic defects in PbTe, such as vacancies of Pb and Te or substitution of a Pb atom by a Te atom and *vice versa*.[34] Therefore, we consider the doping of Bi (n-type) and Na (p-type) simultaneously with internal defects. Fig. 2b shows the correlation between $(C_{12} - C_{44})/B$ and the Pugh ratio for Bi-doped PbTe with the presence of different internal defects. In the case of Bi doping, only the Pb vacancy leads to embrittlement of PbTe (vac_{Pb}, open □ in Fig. 2b), while other types of intrinsic defects do not significantly affect the properties of Bi-

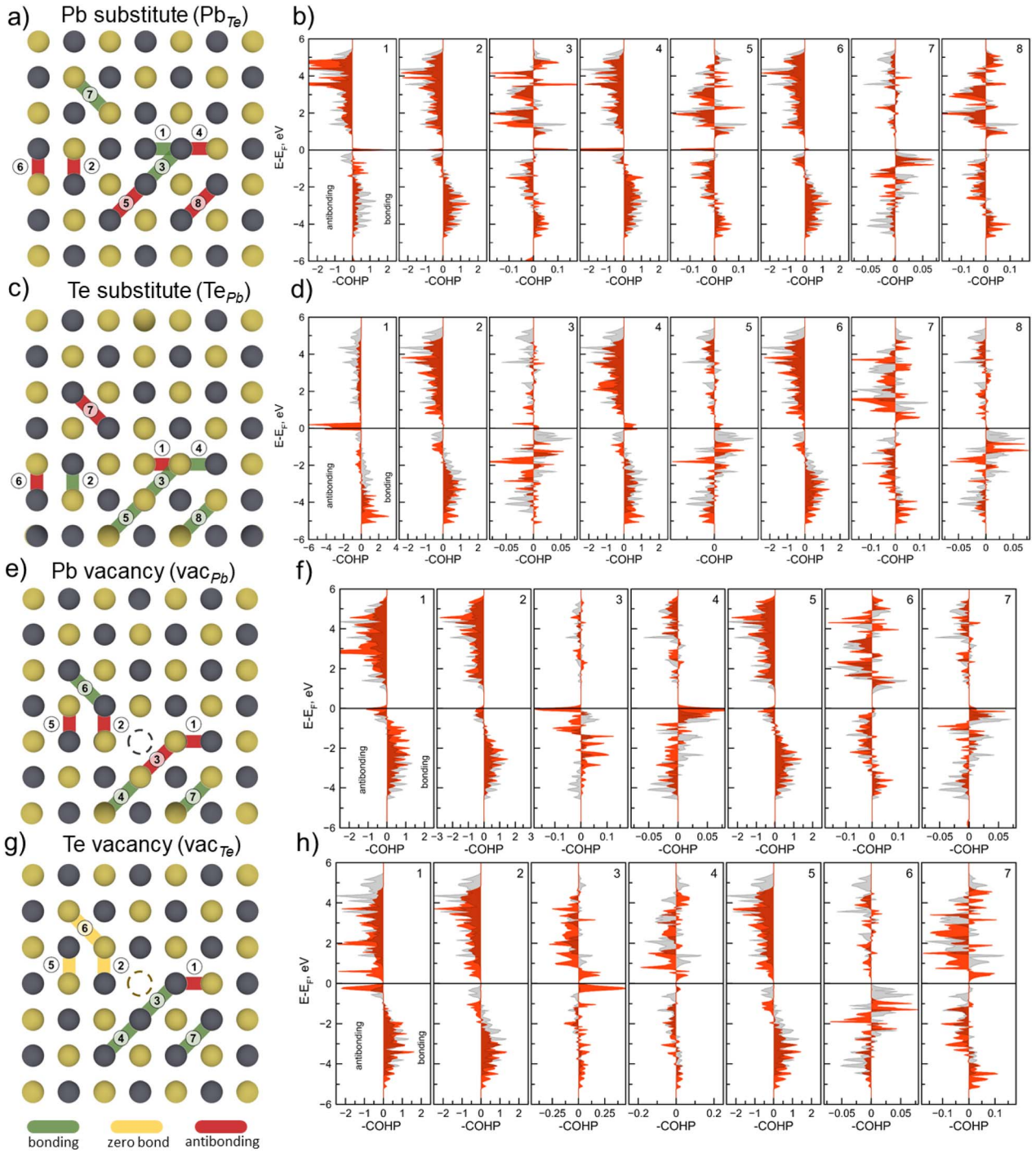

Fig. 3 (a and b) Graphical representation of the bonding and antibonding interactions in PbTe with Pb_{Te} and Te_{Pb} substitution. (c and d) Projected −COHP for each bond, related to Pb_{Te} or Te_{Pb}. (e and f) Graphical representation of the bonding and antibonding interactions in PbTe with Pb and Te vacancies. (g and h) Projected −COHP for each bond, related to Pb or Te vacancies. Grey color corresponds to the −COHP of the Pb–Te bond in undoped PbTe.

doped PbTe. The difference in Pugh ratios is not more than 2%, and in $(C_{12} - C_{44})/B$, the difference does not exceed 17%.

In the case of Na-doped PbTe (Fig. 2c), internal defects, such as Pb_{Te} and vac_{Te} lead to greater ductility than in the case of the single defect of the Na-dopant. In contrast, internal defects Te_{Pb} and vac_{Te} (open △ and ◇ in Fig. 2c) lead to embrittlement of Na-doped PbTe. These results are in agreement with experimental data,[32,33] where it was shown that internal defects Te_{Pb} and vac_{Te} in Na-doped PbTe harden the material and make it more brittle. The solidification mechanism of Na-doped PbTe with Te_{Pb} and vac_{Te} defects has not been explained experimentally.[17] Calculated values of the elastic constants and elastic moduli are presented in Table S1–S8 in the SI.

Another way of tuning mechanical properties is to add interstitial dopants of Ag and Cu (see Fig. 1), which requires a detailed study. For this type of doping, correlations between $(C_{12} - C_{44})/B$ and the Pugh ratio for different concentrations of defects are calculated, as shown in Fig. 2d. It is clearly seen that the ductility of PbTe increases as the Ag/Cu concentration increases from 1 to 5 atoms per cell (216 atoms). It has been shown experimentally that Ag or Cu interstitials themselves have low doping efficiencies and require high concentrations of additional intrinsic defects such as vac_{Pb}.[30,31] Therefore, the interstitial doping of Ag/Cu with different intrinsic defects is considered below. Fig. 2e and f show correlations between $(C_{12} - C_{44})/B$ and the Pugh ratio for interstitial doping of Ag/Cu with Te_{Pb}, Pb_{Te}, vac_{Pb} and vac_{Te} defects. It follows from our calculations that interstitial doping of Ag/Cu with vac_{Pb} defects leads to the same effect of embrittlement as was observed in the experiments.[17]

To understand the influence of different types of defects (substitution, vacancy and interstitial) on bonding in the PbTe crystal, we use the crystal orbital Hamilton population (COHP) analysis. Fig. 3a and c shows the different interactions considered using COHP in the case of Te substituted for Pb (Fig. 3a) and *vice versa* (Fig. 3c). Different types of interactions are chosen based on crystal directions, types of chemical bond, and the distance between the target atom and its neighbor. Nine interactions are chosen in order to study the changes in bonding caused by these defects. In Fig. 3, green lines indicate strengthened bonds compared to undoped PbTe, the red lines show weakened bonds, and yellow lines indicate the bonds that have not changed. The –COHP analysis shows that the substitution of Te by Pb (Pb_{Te}) leads to the formation of a strong Pb–Pb bond with the formation of bonding states at the Fermi level (panel 1 in Fig. 3b), which is absent in undoped PbTe. This bond is strengthened by the formation of bonding states at the Fermi level. However, other bonds such as 2, 4 and 5 have antibonding states at the Fermi level resulting in PbTe with Pb_{Te} being more ductile (see panels 2, 4, 5 in Fig. 3b). The electron density analysis (Fig. 4a) shows that substitution of Te with Pb (Pb_{Te}) leads to small local redistribution of electron density on Pb–Pb bonds, which forms the bonding state at the Fermi level (panel 1 in Fig. 3b). In contrast, the substitution of Pb with Te (Te_{Pb}) (Fig. 3c) leads to the appearance of a large local excess of electrons on the Te–Te bond (Fig. 4b), forming antibonding states at the Fermi level (panel 1 in Fig. 3d). The other bonds become stronger (see panels 2, 3, 4, 5, and 8 in Fig. 3d) and no electron excess is observed there (see Fig. 4b). Such results are additionally confirmed by the atom-resolved band structure for all multiple defects (see Influence of dopants and intrinsic defects on electronic properties section in the SI).

The Pb vacancy (vac_{Pb}) causes a weakening of many of the nearest–neighbour interactions (bonds 1, 2, 3 and 5, shown in red in Fig. 3e) since the Te atoms are left with an unrealized excess electron density due to the impossibility of forming a habitual bond (see Fig. 4c). The additional electrons filled the antibonding states, hence, significant peak in the antibonding

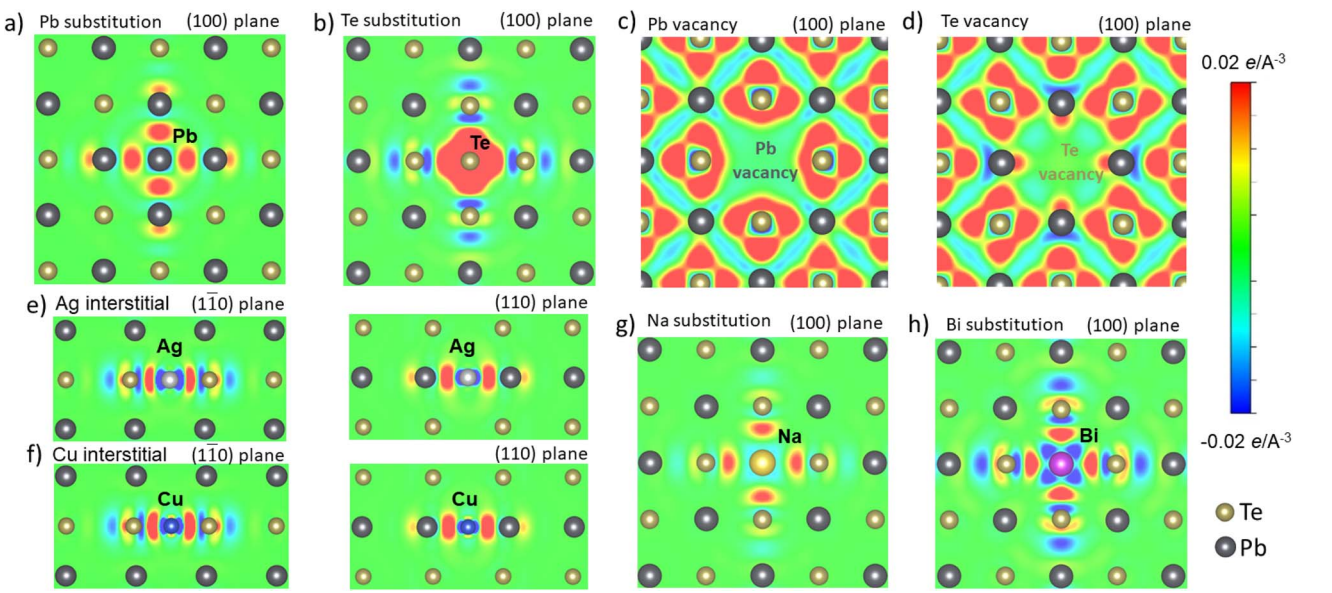

Fig. 4 Charge difference in PbTe with substitution of Pb by Te and *vice versa* (a and b), two types of vacancies: Pb and Te (c and d), Ag and Cu interstitial doping (e and f), and substitution of Pb by Na and Bi (g and h). Red areas correspond to density build-up, whereas blue.

area could be observed for each of –COHP for all of these bonds (bonds 1, 2, 3 and 5, shown by red in Fig. 3f). Despite the fact that the Te vacancy (vac_{Te}) has no significant effect on the nearest–neighbour interactions, it only slightly weakens the closest Pb–Te bonds (bond 1, shown in red in Fig. 3g). The weakening of this bond could be approved by the appearance of the peak in the antibonding area (Fig. 3h). Nevertheless, the electron density redistribution (see Fig. 4d) responsible for this slight weakening has a significant effect on the mechanical strength of the whole material. This is because the combination of vacancy and weak bond (due to the lack of electrons on Pb atoms near the vacancy) could be the cause of brittle fracture. For different concentrations of Pb and Te vacancies, the correlations between $(C_{12} - C_{44})/B$ and the Pugh ratio are calculated as shown in Fig. S1 in the SI. Our calculations show that PbTe with Pb vacancies is more plastic than that with Te vacancies (see Fig. S1 in the SI). It is worth noting that in the case of doping a Pb-rich material (due to the Te vacancy) with a p-type dopant such as Na, which causes the embrittlement of the material, the overall effect of the vacancy and doping is to increase the hardness of such a material.

The same effect is observed in the case of the intrinsic defects such as Ag and Cu interstitials (see Fig. 5a–d). Such impurities provide additional electron density in this area (see Fig. 4e and f), which occupies the antibonding states between Pb and Te atoms and weakens the bonds in the material (bonds 1, 2, 4, 6, and 8 shown in red in Fig. 5b and d), making it more brittle. Thus, by analyzing the –COHP graphs, the antibonding peak in the negative part of the Fermi level could be observed for each of the weakened bonds. At the same time, a new chemical bond is formed between the Pb atoms and the impurity, allowing the impurity to remain in the interatomic space without displacing other atoms. Thus, the combination of the weakening effect of interstitial dopants with the Te-rich material full of Pb vacancies and, as a consequence, the additional electron density, would also change the mechanical properties of the material due to the excess of additional electron density.

In the case of Bi and Na doping, different trends in bond changes are observed. Considering the most important bonds, namely 1 and 4 (see Fig. 5e–h), where a substitution defect is placed instead of Pb, it is found that in the case of doping with an n-type impurity (Bi), the electron excess provokes a shift of the interaction towards antibonding (see Fig. 5h). The increased electron density affects all interactions close to the dopant, resulting in weakening of bonds 2 and 3 as well. Conversely, when doped with a p-type impurity such as Na, the deficiency of electrons leads to only a minimal change in bond 1 (see Fig. 5f). Meanwhile, the 'extra' electrons that are not involved in this bond are redirected to bond 4, weakening this interaction. A similar situation is observed for bonds 2, 3, and 8 (see Fig. 5f). More details about the change in ductility and brittleness of doped-PbTe are explained in our previous research.[25]

The maximum embrittlement of PbTe is observed for the combination of (1) p-type Na-doping with intrinsic defects such as Te vacancies, and (2) n-type Bi-doping (or interstitial dopants such as Ag and Cu) together with intrinsic Pb vacancies. This is explained by consideration of electron density redistribution. In the case of Pb-rich PbTe (p-type doping), the lack of electron density causes the formation of strong bonds, which could break under high mechanical stress. This would make the material hard but brittle. In the case of Te-rich PbTe with Ag or Cu interstitials, there is a significant amount of additional electron density, which causes the Pb–Te bonds to weaken, making it more ductile. The other combinations of doping with intrinsic defects would not have such a strong effect on the mechanical strength of PbTe because of the compensation of electron density from different defects. For example, the extra electron density from n-type doping could compensate for the lack of electron density in Pb-rich PbTe, so embrittlement would be less pronounced. Also, in the case of p-type doping (Na) combined with the Pb vacancy, the additional electron density of the vacancy would compensate for the destructive influence of the Na doping and make the material more stable.[29] Therefore, the concentration of p-type doping can be higher in the Te-rich material without significantly affecting its brittleness.

To obtain deep insight into the changes in mechanical behavior of doped PbTe, we perform the large-scale molecular dynamics simulations using deep neural networks for the description of interatomic interactions in doped PbTe. The high brittleness of Na-doped PbTe is a significant barrier to the commercial use of PbTe-based thermoelectric materials. Therefore, the change in mechanical behaviour of Na-doped PbTe with different intrinsic defect concentrations (vac_{Te}, vac_{Pb}, Pb_{Te}, and Te_{Pb}) is studied in detail. The strain is applied to PbTe nanowires with a constant strain increment of 0.02 Å. Such a small step allows for smooth changes in the atomic structure with the ability to define the variation in ductility and brittleness *via* changes in defect type and concentration.

First, the effect of different vacancy concentrations on the mechanical behavior is investigated. The atomic structure of the Na-doped PbTe nanowire is shown in Fig. 6a, where the types of considered defects are explicitly identified. The main deformation scheme is shown in Fig. 6b and c. We simulate the strain of nanowires with a length of 200 Å and a diameter of 50 Å up to the critical deformation when the nanowire breaks (see Fig. 6c). Obtained stress–strain diagrams for Na-doped PbTe with two types of vacancy defects, namely Te- and Pb-vacancies (vac_{Te} and vac_{Pb}), are shown in Fig. 6d. These types of defects give Na-doped PbTe a more brittle and ductile behavior according to the COHP analysis. The left-hand side of Fig. 6d shows the initial structure (i) and the final structure (ii), after critical deformation, of 2% Na-doped PbTe. These structures are associated with the corresponding points in the stress–strain diagrams in Fig. 6d.

Regarding point (ii), a clear fracture formation can be observed, followed by the sliding of different parts of the wire with respect to each other. The introduction of 2% Te vacancies (see the red curve in the stress–strain diagram in Fig. 6d) results in a decrease in the slope of the elastic region, with noticeable fracture formation occurring at approximately 3.7% strain (point (iii)). As the concentration of vacancies increases, a smoother transformation of the atomic structure is observed

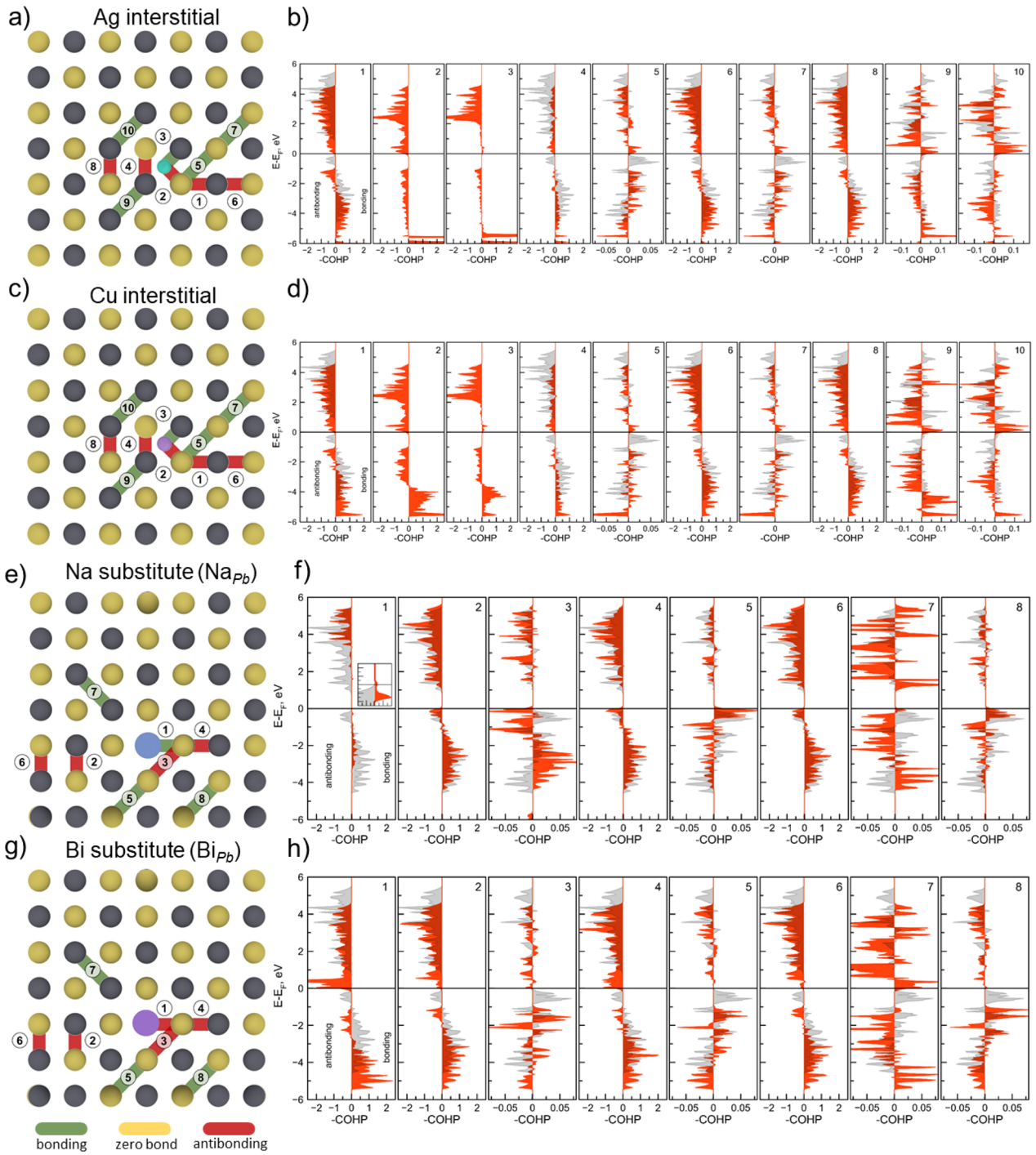

Fig. 5 (a and b) Graphical representation of the bonding and antibonding interactions in PbTe with interstitial doping of Ag/Cu. (c and d) Projected −COHP for each bond, related to the doping of the Ag/Cu atom. (e and f) Graphical representation of the bonding and antibonding interactions in PbTe with substitution of Pb by Bi (n-type) and Na (p-type). (g and h) Projected −COHP for each bond, related to the doping of the Bi/Na atom. Grey color corresponds to the −COHP of the Pb−Te bond in undoped PbTe.

(see point (iv)). A 2% Pb vacancy concentration forms a smoother fracture interface (Fig. 6d, point (v), red curve). A further increase in vacancies enhances the defectiveness of PbTe, reducing the elastic constant and subsequently decreasing the critical strain to less than 4%.

Other defect types such as Pb_{Te} and Te_{Pb} will affect the mechanical properties in different ways. Pb substitution contributes to an increase in ductility, whereas Te substitution makes Na-doped PbTe more brittle, as can be seen from Fig. 7. Initial structures with 4 and 6% of Pb substitutions correspond to the points (i) and (ii) in Fig. 7a. The presence of 4% of Pb substitutional defects (see the magenta line in Fig. 7a) leads to a decrease in the slope of the elastic region, which is associated with a decrease in the elastic constant of the wire. The

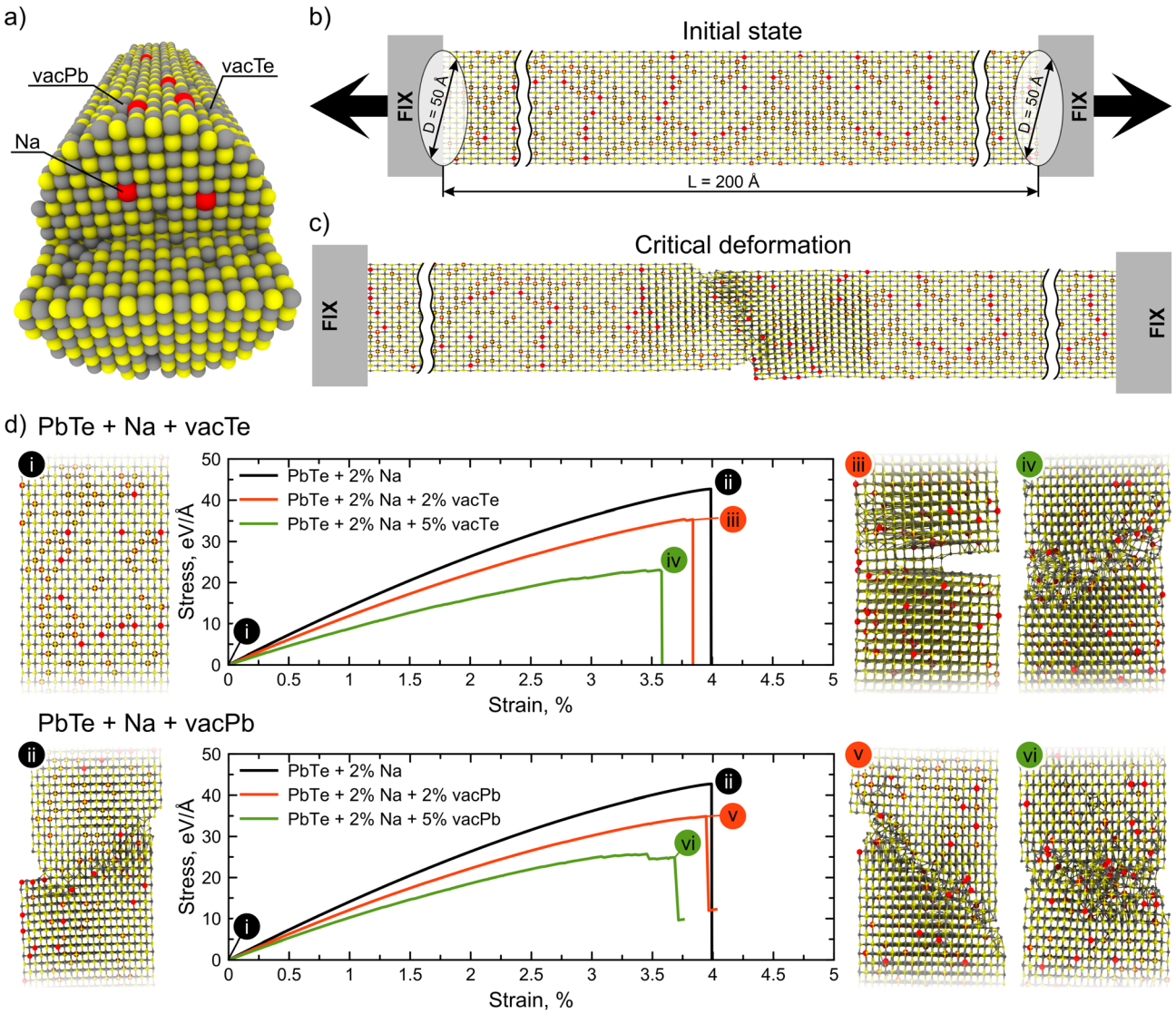

Fig. 6 (a) Perspective view of a cylinder used for simulations of critical deformations in doped PbTe with indicated defects. Principal scheme of simulation including (b) the initial undeformed state and (c) the state under critical deformation. (d) Stress–strain relations calculated for Na-doped PbTe with different concentrations of Te and Pb vacancies as intrinsic defects. Roman numbers on the plot correspond to the deformed structures at special strain ratios: (i) is the initial undeformed structure of 2% Na-doped PbTe with various Te/Pb vacancies (marked by color); (ii) is the atomic structure at the critical strain of Na-doped PbTe without vacancies. The atomic structures of Na-doped PbTe at the critical strain for Te (iii and iv) and Pb (v and vi) vacancies. Red and green colors correspond to 2% and 5% of Te (top) and Pb (bottom) vacancy concentrations. Sodium substitutions are shown in red, Pb in yellow, and Te in gray.

apparently flatter behavior (from 1.5% strain) indicates a transition to plastic deformation in the yield region of the material. The smooth changes in the atomic structure of Na-doped PbTe with Pb substitutions during deformation are observed from the simulation snapshots from point (i) to point (v). Starting from point (iv), weak necking can be observed, followed by plastic atomic structure transformation with a transverse size decrease.

A similar situation is observed for the structure with 6% Pb substitution (see cyan color in Fig. 7a). Here, starting from the 3% strain (point (vi)), the plastic deformation behavior is clearly observed with subsequent necking at point (vii). In contrast, 4% Te substitution acts as a factor increasing the brittleness of Na-doped PbTe. The stress–strain curves for Te substitutional defects are shown in Fig. 7b. 2% Te substitution leads to fracture formation even at stress less than 3% (see red line, point (iv)). Increasing the substitution concentration to 4% leads to the appearance of yield point strain during which dislocation formation is observed, (v) → (vi) → (vii). No smooth structural transformation is observed as in the case of Pb substitution in Fig. 7a. A similar situation is observed with further increase of Te substitution defects (6%, cyan color, point (viii)).

Other types of defects, such as interstitials (Ag and Cu), are considered, and the behavior under mechanical stress in a combination with other dopants is analyzed. The main contribution to the embrittlement behavior comes from the incorporation of interstitial impurities. Detailed description

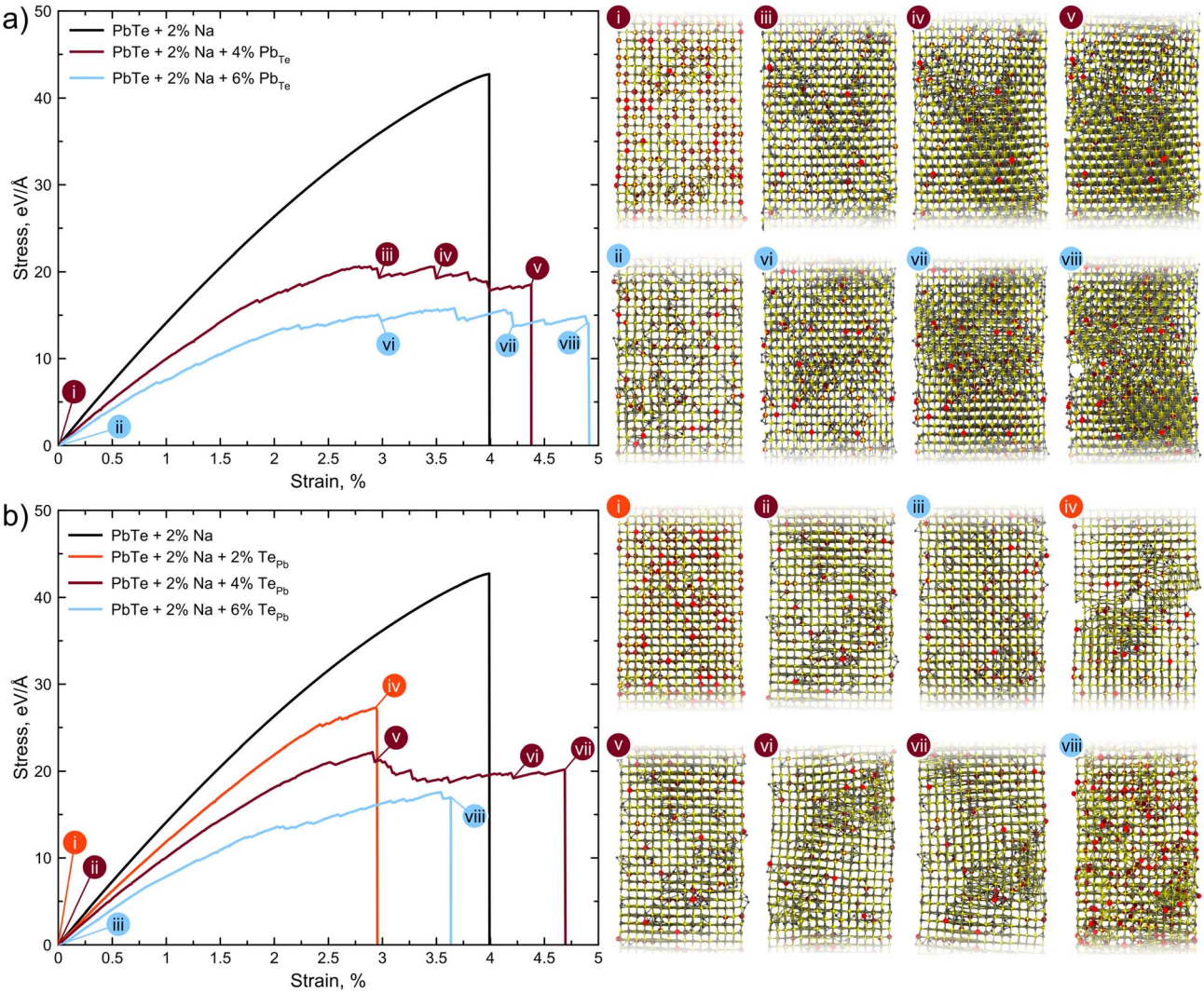

Fig. 7 Stress–strain relations calculated for Na-doped PbTe with different concentrations of intrinsic defects, namely substitution of (a) Pb by Te, and (b) Te by Pb. (a) Roman numbers on the plot correspond to the deformed structures at special strain ratios: (i) and (ii) are the initial undeformed structure of 2% Na-doped PbTe with Pb substitution defects of various concentrations (marked by color). (iii)–(v) and (vi) and (vii) are the atomic structure at significant points and at the critical strain ratio of Na-doped PbTe with 4% and 6% of Pb substitution defects (brown and cyan color). (b) (i)–(iii) are the initial undeformed structures of 2% Na-doped PbTe with Te substitution defects of various concentrations (2%, 4% and 6% marked by color). (iv), (vii) and (viii) are the atomic structures at the critical strain ratio of Na-doped PbTe with 2%, 4% and 6% of Te substitution defects (orange, brown and cyan colors). (v) and (vi) are the significant strain ratio structures. Sodium substitutions are shown in red, Pb in yellow, and Te in gray.

together with calculated stress–strain curves are presented in the SI. The influence of the temperature on the mechanical properties of Ag/Cu-doped PbTe is studied, and stress–strain curves calculated at 300 K in comparison with 0 K data are shown in Fig. S8 in the SI.

Thus, using large-scale simulation with deep neural network potentials, we show how different types of intrinsic defects can tune the mechanical behavior of PbTe thermoelectric materials. The brittleness of Na-doped PbTe, which poses significant commercial challenges, can be mitigated by introducing a small concentration of intrinsic defects such as vac_{Pb} and Pb_{Te}. In the case of Ag and Cu interstitials, tuning is complicated by the fact that Ag/Cu atoms are embedded in the interatomic space, but large concentrations (more than 4–6%) of Pb_{Te} (for Ag and Cu) and Te_{Pb} (for Ag) can make PbTe thermoelectric materials more ductile.

Finally, we note that the generation of defects should not substantially decrease the thermoelectric figure of merit of the aforementioned structures. Evaluation of the charge transport goes beyond the scope of this paper, since it requires large-scale electronic structure calculations.[56] In contrast, generation of defects should definitely affect phonon scattering processes and lead to the decrease of the thermal conductivity.[57] To confirm this, we perform calculations of the lattice thermal conductivity (LTC) using the Green–Kubo method. We use the moment tensor potential model for these calculations.[53,54,58–60] The obtained results are shown in Fig. S10 in the SI. It is found that the addition of any type of defects leads to a reduction in lattice thermal

conductivity. It is shown that Na-doping results in a 30% reduction in LTC, while the addition of substitutional Pb defects leads to an even more significant reduction of LTC by 67%. A similar situation is observed for Cu-doping, where the maximum reduction in LTC is attributed to substitutional Te defects.

4 Conclusion

In conclusion, we perform a comprehensive study of the influence of different types of intrinsic defects, such as substitutions, vacancies and interstitials, on chemical bonding in doped PbTe thermoelectric materials. Our calculations show a pronounced embrittlement for Na-doped PbTe (p-type) with Te-vacancies (vac_{Te}), which are intrinsic defects in PbTe. The same behavior is observed with Ag/Cu interstitials (n-type) together with Pb vacancies (vac_{Pb}), which is in agreement with known experimental data. A detailed study of chemical bonding in PbTe crystals using the Crystal Orbital Hamilton Population (COHP) analysis allows us to define the origin of the brittle behavior of doped PbTe with different types of intrinsic defects. The crucial factor influencing the variation of brittleness and ductility of doped PbTe with different types of intrinsic defects is the excess or deficiency of electron density on the bonds inside PbTe. Deep neural network simulations reveal optimal tuning mechanisms for improving the mechanical behavior of doped PbTe. For example, it is defined that Na-doped PbTe can be made more ductile by a small percentage of intrinsic defects such as vac_{Pb} and Pb_{Te}. The p-type Ag/Cu-doped PbTe can be made more ductile by intrinsic defects such as Pb_{Te} (for Ag and Cu) and Te_{Pb} (for Ag). In addition, we perform molecular dynamics simulations with moment tensor potentials and computed lattice thermal conductivity using the Green–Kubo method to confirm that heat transport properties of the PbTe structures with vacancies (Pb or Te) and substitutions (Na and Cu) are not affecting their applicability as thermoelectric materials. The obtained results can contribute to the design and development of high-efficiency thermoelectric generators based on PbTe, overcoming their main disadvantage related to mechanical brittleness.

Author contributions

Conceptualization: I. V. C. and Z. D. Writing – original draft: I. V. C., A. D. R., D. G. K., and A. G. K. Investigation: I. V. C., A. D. R., B. V. S., M. P., A. A. K., A. R. O., N. R., A. S., D. G. K., and A. G. K. Writing – review & editing: A. G. K. and I. V. C. Supervision: A. G. K.

Conflicts of interest

There are no conflicts to declare.

Data availability

The moment tensor potentials were generated using MLIP-2 package, which is available at **https://mlip.skoltech.ru/download/**. SI contains the results of lattice thermal conductivity calculations and the accompanying gitlab repository (**https://github.com/tregedron/Na-and-Cu-doped-PbTe**) contains MTP potentials and training sets.

Additional data on mechanical properties of PbTe with considered types of defects, stress–strain curves, temperature dependent stress–strain curves, details about lattice thermal conductivity, and electronic band structures of all doped PbTe crystals. See DOI: **https://doi.org/10.1039/d5ta00823a**.

Acknowledgements

The research was carried out using the resources of the Center for the Information and Computing of Novosibirsk State University and Zhores supercomputers at Skoltech. D. G. K. acknowledges financial support from the federal budget of the Russian Ministry of Science and Higher Education, no. 122041400110-4 (description of the results of mechanical properties depending on the type and concentration of defects, atom-resolved band structures, analysis and description of the dependencies of formation energy on deformation). V. S. B acknowledges funding from the Russian Science Foundation no.25-73-20094 **https://rscf.ru/en/project/25-73-20094/** (training ML potentials (DeepMD) for different types of chemical bonding). M. P., N. R., and A. S. acknowledge funding from the Russian Science Foundation no.23-13-00332 (Green-Kubo calculations of the LTC). A. A. K. and A. R. O. acknowledge funding from the Russian Science Foundation no.19-72-30043 (DFT calculations of COHP and electronic properties). The atomic structures and electron localization functions (ELF) are illustrated using the VESTA package.[61]

Notes and references

1 Y. Xiao and L.-D. Zhao, *npj Quantum Mater.*, 2018, **3**, 55.
2 Y. Xiao and L.-D. Zhao, *Science*, 2020, **367**, 1196–1197.
3 S. Liu, Y. Qin, Y. Wen, H. Shi, B. Qin, T. Hong, X. Gao, Q. Cao, C. Chang and L.-D. Zhao, *Adv. Funct. Mater.*, 2024, 2315707.
4 O. Delaire, J. Ma, K. Marty, A. F. May, M. A. McGuire, M.-H. Du, D. J. Singh, A. Podlesnyak, G. Ehlers, M. Lumsden, *et al.*, *Nat. Mater.*, 2011, **10**, 614–619.
5 A. D. LaLonde, Y. Pei, H. Wang and G. J. Snyder, *Mater. Today*, 2011, **14**, 526–532.
6 Y. Zhong, J. Tang, H. Liu, Z. Chen, L. Lin, D. Ren, B. Liu and R. Ang, *ACS Appl. Mater. Interfaces*, 2020, **12**, 49323–49334.
7 O. Khshanovska, T. Parashchuk and I. Horichok, *Mater. Sci. Semicond. Process.*, 2023, **160**, 107428.
8 Z. Dashevsky and S. Skipidarov, *Novel Thermoelectric Materials and Device Design Concepts*, 2019, 3–21.
9 N. Sidorenko, Y. Unigovski, Z. Dashevsky and R. Shneck, *Electron. Mater.*, 2021, **2**, 511–526.
10 Z. Dashevsky, I. Horichok, M. Maksymuk, A. R. Muchtar, B. Srinivasan and T. Mori, *J. Am. Ceram. Soc.*, 2022, **105**, 4500–4511.
11 A. Sorokin, M. Ivantsov, N. Y. Tabachkova, V. Bublik, S. Y. Skipidarov and Z. Dashevsky, *Semiconductors*, 2022, **56**, 16–20.

12 C. Qin, L. Cheng, Y. Xiao, C. Wen, B. Ge, W. Li and Y. Pei, *Mater. Today Phys.*, 2021, **17**, 100355.
13 X. Hao, X. Chen, X. Zhou, L. Zhang, J. Tao, C. Wang, T. Wu and W. Dai, *Front. Energy Res.*, 2021, **9**, 754532.
14 S. Mamykin, R. Z. Shneck, B. Dzundza, F. Gao and Z. Dashevsky, *Energies*, 2023, **16**, 3036.
15 M. M. A. Malki, G. J. Snyder and D. C. Dunand, *Int. Mater. Rev.*, 2023, **68**, 1050–1074.
16 J. P. Male, R. Hanus, G. J. Snyder and R. P. Hermann, *Chem. Mater.*, 2021, **33**, 4765–4772.
17 J. P. Male, L. Abdellaoui, Y. Yu, S. Zhang, N. Pieczulewski, O. Cojocaru-Mirédin, C. Scheu and G. J. Snyder, *Adv. Funct. Mater.*, 2021, **31**, 2108006.
18 B. Huang, G. Li, B. Duan, W. Li, P. Zhai and W. A. Goddard III, *ACS Appl. Mater. Interfaces*, 2021, **13**, 57629–57637.
19 G. M. Guttmann and Y. Gelbstein, *Bringing Thermoelectricity into Reality*, 2018, 63–80.
20 G. Li, U. Aydemir, B. Duan, M. T. Agne, H. Wang, M. Wood, Q. Zhang, P. Zhai, W. A. Goddard III and G. J. Snyder, *ACS Appl. Mater. Interfaces*, 2017, **9**, 40488–40496.
21 Y. Li, X. Liu, J. Liu and C. Wan, *Appl. Phys. Lett.*, 2023, **123**, 183905.
22 P. Sauerschnig, P. Jood and M. Ohta, *Adv. Mater. Technol.*, 2023, **8**, 2201295.
23 M. M. Al Malki, G. J. Snyder and D. C. Dunand, *Int. Mater. Rev.*, 2023, **68**, 1050–1074.
24 Y. Gelbstein, G. Gotesman, Y. Lishzinker, Z. Dashevsky and M. Dariel, *Scr. Mater.*, 2008, **58**, 251–254.
25 I. V. Chepkasov, A. G. Kvashnin, A. D. Radina, N. A. Matsokin, F. N. Jalolov, D. G. Kvashnin, A. R. Oganov and Z. Dashevsky, *Appl. Phys. Lett.*, 2024, **124**, 022104.
26 A. Goyal, P. Gorai, E. S. Toberer and V. Stevanović, *npj Comput. Mater.*, 2017, **3**, 42.
27 X. Zhang, M. Y. Toriyama, J. P. Male, Z. Feng, S. Guo, T. Jia, Z. Ti, G. J. Snyder and Y. Zhang, *Mater. Today Phys.*, 2021, **19**, 100415.
28 Z. Chen, B. Ge, W. Li, S. Lin, J. Shen, Y. Chang, R. Hanus, G. J. Snyder and Y. Pei, *Nat. Commun.*, 2017, **8**, 13828.
29 X. Zhao, B. Fu and R. Ang, *ACS Appl. Mater. Interfaces*, 2024, **16**(51), 70685–70693.
30 B. Ryu, M.-W. Oh, J. K. Lee, J. E. Lee, S.-J. Joo, B.-S. Kim, B.-K. Min, H.-W. Lee and S.-D. Park, *J. Appl. Phys.*, 2015, **118**, 015705.
31 Y. Xiao, H. Wu, W. Li, M. Yin, Y. Pei, Y. Zhang, L. Fu, Y. Chen, S. J. Pennycook, L. Huang, *et al.*, *J. Am. Chem. Soc.*, 2017, **139**, 18732–18738.
32 P. Jood, J. P. Male, S. Anand, Y. Matsushita, Y. Takagiwa, M. G. Kanatzidis, G. J. Snyder and M. Ohta, *J. Am. Chem. Soc.*, 2020, **142**, 15464–15475.
33 J. W. Doak, K. J. Michel and C. Wolverton, *J. Mater. Chem. C*, 2015, **3**, 10630–10649.
34 F. Lv, Y. Zhong, X. Zhao, X. An, Q. Deng, L. Gan, L. Lin and R. Ang, *Small*, 2023, **19**, 2301352.
35 J. F. Troncoso, P. Aguado-Puente and J. Kohanoff, *J. Phys.: Condens. Matter*, 2019, **32**, 045701.
36 X. Zhao, B. Fu and R. Ang, *Adv. Funct. Mater.*, 2024, 2401582.
37 X. Zhao, B. Fu and R. Ang, *Appl. Phys. Lett.*, 2025, **126**, 043901.
38 G. Kresse and J. Furthmüller, *Phys. Rev. B: Condens. Matter Mater. Phys.*, 1996, **54**, 11169.
39 G. Kresse and D. Joubert, *Phys. Rev. B: Condens. Matter Mater. Phys.*, 1999, **59**, 1758.
40 G. Kresse and J. Furthmüller, *Comput. Mater. Sci.*, 1996, **6**, 15–50.
41 J. P. Perdew, A. Ruzsinszky, G. I. Csonka, O. A. Vydrov, G. E. Scuseria, L. A. Constantin, X. Zhou and K. Burke, *Phys. Rev. Lett.*, 2008, **100**, 136406.
42 L. A. Constantin, J. M. Pitarke, J. Dobson, A. Garcia-Lekue and J. P. Perdew, *Phys. Rev. Lett.*, 2008, **100**, 036401.
43 H. J. Monkhorst and J. D. Pack, *Phys. Rev. B: Condens. Matter Mater. Phys.*, 1976, **13**, 5188.
44 O. Senkov and D. Miracle, *Sci. Rep.*, 2021, **11**, 4531.
45 M. T. Ruggiero, A. Erba, R. Orlando and T. M. Korter, *Phys. Chem. Chem. Phys.*, 2015, **17**, 31023–31029.
46 V. L. Deringer, A. L. Tchougréeff and R. Dronskowski, *J. Phys. Chem. A*, 2011, **115**, 5461–5466.
47 S. Plimpton, *J. Comput. Phys.*, 1995, **117**, 1–19.
48 A. P. Thompson, H. M. Aktulga, R. Berger, D. S. Bolintineanu, W. M. Brown, P. S. Crozier, P. J. In't Veld, A. Kohlmeyer, S. G. Moore, T. D. Nguyen, *et al.*, *Comput. Phys. Commun.*, 2022, **271**, 108171.
49 Y. Zhang, H. Wang, W. Chen, J. Zeng, L. Zhang, H. Wang and E. Weinan, *Comput. Phys. Commun.*, 2020, **253**, 107206.
50 V. S. Baidyshev, C. Tantardini and A. G. Kvashnin, *Sci. Rep.*, 2024, **14**, 28678.
51 D. S. Nikitin, I. I. Shanenkov, A. R. Nassyrbayev, A. A. Sivkov, V. S. Baidyshev, Y. A. Kvashnina, N. A. Matsokin, A. Y. Pak and A. G. Kvashnin, *J. Alloys Compd.*, 2025, **1010**, 177178.
52 H. Wang, L. Zhang, J. Han and W. E, *Comput. Phys. Commun.*, 2018, **228**, 178–184.
53 A. V. Shapeev, *Multiscale Model. Simul.*, 2016, **14**, 1153–1173.
54 I. S. Novikov, K. Gubaev, E. V. Podryabinkin and A. V. Shapeev, *Mach. Learn.: Sci. Technol.*, 2020, **2**, 025002.
55 E. V. Podryabinkin and A. V. Shapeev, *Comput. Mater. Sci.*, 2017, **140**, 171–180.
56 J. Quan, C. Carbogno and M. Scheffler, *Phys. Rev. B*, 2024, **110**, 235202.
57 J. M. Ziman, *Electrons and Phonons: the Theory of Transport Phenomena in Solids*, Oxford university press, 2001.
58 N. Rybin and A. Shapeev, *J. Appl. Phys.*, 2024, **135**, 205108.
59 B. Mortazavi, E. V. Podryabinkin, I. S. Novikov, T. Rabczuk, X. Zhuang and A. V. Shapeev, *Comput. Phys. Commun.*, 2021, **258**, 107583.
60 S. T. Tai, C. Wang, R. Cheng and Y. Chen, *J. Chem. Theory Comput.*, 2025, **21**, 3649–3657.
61 K. Momma and F. Izumi, *J. Appl. Crystallogr.*, 2008, **41**, 653–658.

